analytical chemistry

pubs.acs.org/ac Article

Parts-per-Million Detection of Trace Crystal Forms Using AF-PTIR Microscopy

Aleksandr Razumtcev,[†] Minghe Li,[†] and Garth J. Simpson*

Cite This: *Anal. Chem.* 2022, 94, 13100−13107 Read Online

ACCESS | Metrics & More | Article Recommendations | Supporting Information

ABSTRACT: Autofluorescence-detected photothermal mid-infrared (AF-PTIR) microscopy was shown to enable parts-per-million detection of α-indomethacin impurity in γ-indomethacin samples. Subtle differences in the photothermal response of the UV-autofluorescence of two indomethacin crystal polymorphs were used for sub-micron chemical discrimination based on fingerprint region mid-IR spectroscopy. The AF-PTIR assignment was independently confirmed by second harmonic generation (SHG) microscopy, which was shown to reduce the total analysis time by rapidly identifying the suitable fields of view. AF-PTIR microscopy has the potential to assist in the early identification of crystal form impurities in the solid dosage forms development pipeline.

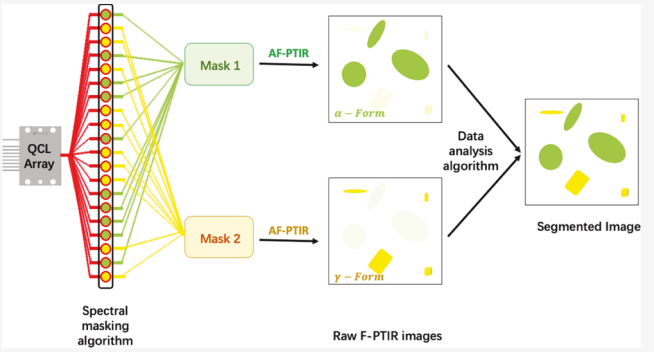

INTRODUCTION

Crystal polymorphism of active pharmaceutical ingredients (APIs) plays a crucial role in dosage form development, licensing, and commercial distribution. Roughly half of all APIs on the market can exist in multiple crystal forms.[1] Different crystal forms of the same therapeutic compound often have drastically different dissolution kinetics, affecting bioavailability.[2,3] The more thermodynamically stable crystal forms tend to have lower apparent aqueous solubility, motivating pharmaceutical companies to use alternative formulation designs such as amorphous solid dispersions (ASDs) of APIs to overcome solubility limitations. The presence of trace amounts of low soluble crystal forms can lead to crystallization nuclei formation and conversion of metastable polymorph crystals.[4,5] Therefore, pharmaceutical companies go to extensive lengths to identify and characterize all accessible stable polymorphs and crystal forms of newly developed chemical entities that might outcompete known forms. One of the most notable examples of crystal polymorphism in APIs is ritonavir, used as the active ingredient in formulations for HIV antiretroviral therapy. The most thermodynamically stable crystal form of ritonavir (form II) was not discovered during the initial development and production of the commercial final dosage form. Its subsequent emergence resulted in lower bioavailability and a temporary recall of the product for reformulation.[6] Furthermore, early identification of multiple accessible polymorphs is vital for patent protection in the event that formulations with particular crystal forms exhibit enhancement in stability and/or bioavailability within final dosage forms. In polymorph screening protocols, it may be challenging to rapidly identify new crystal forms present at trace quantities, particularly if a given set of conditions produces multiple crystal forms under kinetic control.

Many analytical techniques have been used for the sensitive detection of trace crystalline phases. X-ray diffraction remains the "gold standard" nondestructive method for the characterization of crystalline APIs due to its inherent selectivity to different crystal forms. However, the detection limit of powder X-ray diffraction (PXRD) is on the order of 1% for most commercially available instruments.[7] Synchrotron powder X-ray diffraction was shown to lower the limit of detection (LoD) by an order of magnitude.[8] However, synchrotron facilities are not easily accessible and are challenging for routine analysis. Alternative techniques that were applied to analyze low volume fractions of crystalline materials include differential scanning calorimetry (DSC) and Raman techniques. However, LoDs of these methods are typically similar to what can be achieved using conventional PXRD.[9−12] Detection limits of such bulk sampling methods might be insufficient to confidently detect trace impurities of undesired crystal forms during the formulation development and production, which might lead to product withdrawal and potential need for reformulation.

Chemically specific microscopy has generally been quite successful in further reducing the limits of detection. By performing localized analysis, the corresponding reduction in

Received: June 2, 2022
Accepted: August 31, 2022
Published: September 13, 2022

https://doi.org/10.1021/acs.analchem.2c02358
Anal. Chem. 2022, 94, 13100−13107

the background can greatly improve sensitivity to trace components. For instance, second harmonic generation (SHG) microscopy provides some promising opportunities when applied to ultrasensitive detection of crystalline APIs of appropriate symmetry. At optical wavelengths, SHG microscopy is uniquely selective for noncentrosymmetric ordered molecular assemblies, as coherent SHG is symmetry-forbidden in centrosymmetric and/or isotropic media.[13,14] As such, SHG can provide high contrast for homochiral crystals, with negligible background interference from amorphous media. In a survey of small molecule APIs, Toth and co-workers demonstrated that a significant fraction of commercially available API crystals generates SHG signal due to the ubiquity of homochiral molecules among novel drug candidates.[15] However, despite its high selectivity toward noncentrosymmetric crystals, SHG microscopy alone provides little information on the chemical composition of studied materials. The potential presence of multiple SHG-active analytes can significantly complicate qualitative analysis. Furthermore, even in cases in which SHG can enable crystal form discrimination, confirmation using an independent method can greatly improve statistical confidence. To address these limitations, Newman and co-workers used the high sensitivity and spatial resolution of optical SHG microscopy to perform SHG-guided synchrotron PXRD analysis, demonstrating that parts-per-million (ppm) limits of detection of trace ritonavir crystals in an amorphous matrix.[16] However, benchtop X-ray sources rarely provide the confinement for localized XRD analysis within <5 μm domains, and access to synchrotron sources can be challenging to secure, particularly for proprietary molecules.

Raman spectroscopy and imaging methods have been employed to enable chemical discrimination based on vibrational signatures with high spatial resolution. Conventional Raman microscopy was shown to enable chemically selective optical microscopy of pharmaceutical ingredients,[17] but spontaneous Raman techniques have relatively low sensitivity due to low cross sections of Raman scattering. Terahertz Raman is more sensitive to intermolecular lattice structure but has found fewer applications in microscopy instrumentation for imaging.[18] Schmitt et al. demonstrated the use of SHG-guided Raman analysis within pharmaceutical samples to reduce the total analysis time for spontaneous Raman microscopy.[19] Coherent Raman microscopy has the potential to address the speed and sensitivity limitations of conventional Raman. Coherent anti-Stokes Raman (CARS) microscopy was demonstrated to enable highly sensitive chemically specific discrimination between crystal forms of different APIs.[20,21] Hartshorn et al. used broadband CARS microscopy to perform a rapid qualitative assessment of pharmaceutical tablets containing a mixture of two crystal forms of anti-inflammatory drug indomethacin.[22] Despite the prior success of Raman for chemical classification with high spatial resolution, the statistical confidence of a chemical assignment is generally improved when multiple independent analysis approaches agree. As such, the development of tools complementary to Raman analysis is highly desirable.

Absorption of mid-IR radiation can be used to perform microspectroscopy measurements and obtain chemical information complementary to Raman techniques due to different selection rules for Raman and IR spectroscopy. Because absorption is a lower-order interaction, it exhibits a weaker dependence on crystal orientation. Furthermore, the mid-infrared "fingerprint" region is well established as being highly sensitive to the weak-intermolecular interactions associated with crystal contacts. However, direct mid-infrared microscopy suffers from low spatial resolution limited by the diffraction of mid-IR light.[23] Most formulations produce particles with sizes around ~1 to 10 μm. Optical photothermal mid-IR microscopy (O-PTIR) was introduced as a technique combining chemical selectivity of the fingerprint region infrared spectroscopy with high spatial resolution enabled by visible optical microscopy.[24,25] O-PTIR is usually performed using an instrument based on co- or counter-propagating visible and mid-infrared laser sources. In this configuration, the probe visible beam is used to detect localized changes in refractive index (dn/dT) induced by mid-IR absorption and the subsequent heating. However, the signal-to-noise characteristics of O-PTIR microscopy are limited by the relatively weak temperature dependence of refractive index (around 10^{-2}% per °C). Furthermore, O-PTIR signal is often biased toward the most scattering particles within a FoV.[26]

Recently, Simpson and co-workers and Cheng and co-workers independently demonstrated a complementary technique employing fluorescence-detected mid-infrared photothermal microscopy (F-PTIR).[27,28] In F-PTIR, temperature-induced changes in fluorescence quantum efficiency (dQ_e/dT) are used to report on local mid-IR absorption rather than changes in the refractive index. Given that the values of dQ_e/dT can routinely be two orders of magnitude higher than the accompanying values of dn/dT, F-PTIR was shown to achieve improved signal-to-noise characteristics compared to O-PTIR. F-PTIR was applied to characterize the chemical composition of phase-separated domains in a ritonavir ASD and to perform chemically selective microscopy of living cells. In follow-up work related to pharmaceutical formulations, Simpson and co-workers used native two-photon excited UV-fluorescence (TPE-UVF) of indomethacin API crystals to perform label-free autofluorescence-detected mid-IR photothermal microscopy (AF-PTIR).[29] AF-PTIR was shown to enable chemical mapping of the indomethacin API crystals within a commercial solid dosage form.

In the present work, AF-PTIR is used to detect trace impurities of α-indomethacin crystals in samples predominantly consisting of crystals of γ-indomethacin. Subtle structural differences associated with internal conformational changes and with differences in crystal contacts produced detectable changes in the "fingerprint" region of the infrared spectra for the α- and γ-crystal forms. Spectral masks were optimized to differentiate between the two different crystal forms by AF-PTIR. The accuracy of assignment by vibrational spectroscopy was assessed by SHG measurements, leveraging the SHG activity of the metastable α-form. Figures of merit, including limits of detection, for AF-PTIR microscopy in trace analysis of crystal polymorphism were critically assessed.

EXPERIMENTAL METHODS

AF-PTIR Instrumentation. The instrumentation supporting AF-PTIR, TPE-UVF, and SHG imaging was described in detail previously.[29] In brief, the microscope system was based on a counter-propagating probe and mid-infrared pump sources (Figure 1). A 1064 nm near-IR femtosecond laser (Fianium FemtoPower; 150 fs pulses at 50 MHz repetition rate and up to 1 W average power at 1064 nm emission) was used for nonlinear imaging. The laser was passed through a second harmonic generation crystal to produce a frequency-doubled visible 532 nm beam that was used for two-photon excitation

https://doi.org/10.1021/acs.analchem.2c02358
Anal. Chem. 2022, 94, 13100−13107

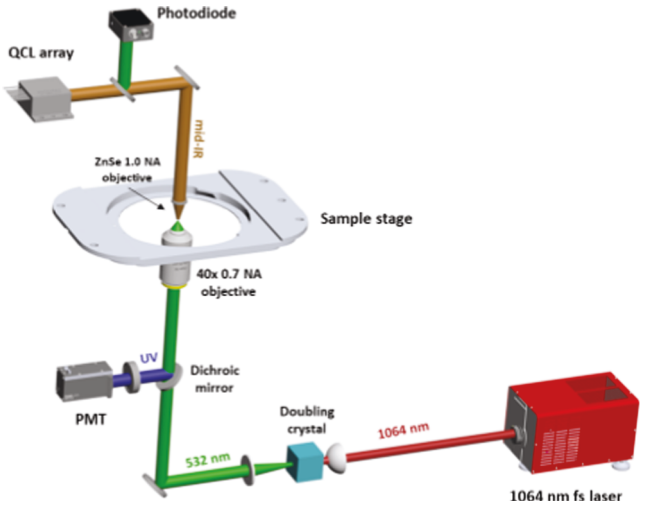

Figure 1. AF-PTIR instrument schematics.

of indomethacin UV-autofluorescence. The average power of the excitation beam at the sample plane was around 3 mW. The fundamental was suppressed by a combination of an absorptive KG3 filter (Thorlabs) with a 530 ± 15 nm band-pass filter (Edmund Optics). The emitted UV-autofluorescence signal was separated from the incident light by a dichroic mirror and optical filters (532 notch (Semrock) + 532 shortpass (Semrock) + 506 shortpass (Edmund Optics)) and collected with a photomultiplier tube (Hamamatsu H10721-210). For SHG imaging, a half-wave plate in front of the doubling crystal was rotated to decrease the conversion efficiency, and the fundamental 1064 beam was used to illuminate the sample and produce SHG. The average incident power for SHG imaging was around 50 mW at the sample plane. The residual 532 nm doubled incident light was filtered out with a notch filter. SHG was collected using the same epi-PMT and separated using a 570 nm longpass dichroic mirror and a set of optical filters (KG3 and 530 ± 15 nm bandpass). Both TPE-UVF and SHG images were collected by sample scanning using a Mad City Labs Nano-Bio 300 piezoelectric sample stage with a maximum scanning range of 300 μm on each axis.

A monolithic array of 32 independent quantum cascade lasers (QCLs) was used as a mid-IR radiation source, spanning a range of energies from 1054 to 1186 cm^{-1}. QCL radiation was delivered and focused to the sample plane with lenses and an aspheric objective made from mid-IR transparent zinc selenide (ZnSe). The QCL array was operated in a burst mode, in which rapid bursts of multiple spectral channels were followed by long quiescent periods, as was described previously.[27] The duty cycle of each QCL was maintained at 1%. Each spectral channel produced 300 ns mid-infrared pulses with a 30 ns delay between adjacent spectral channels within a sequence.

AF-PTIR images were generated by digital processing of the fluorescence signal, following frequency filtering around the QCL modulation frequency using an Ithaco 4302 electronic band-pass filter. The AF-PTIR intensity on each image pixel was calculated by digital lock-in amplification of the filtered fluorescence signal. In brief, the phase-sensitive filtered PMT output was digitized, summed over one modulation period, and fitted to a sine function to recover the modulation amplitude at a fixed phase. This amplitude was mapped as a function of position to generate the photothermal images. The total collection time for each 100 pixels × 100 pixels AF-PTIR image was 300 s, corresponding to a 30 ms pixel dwell time.

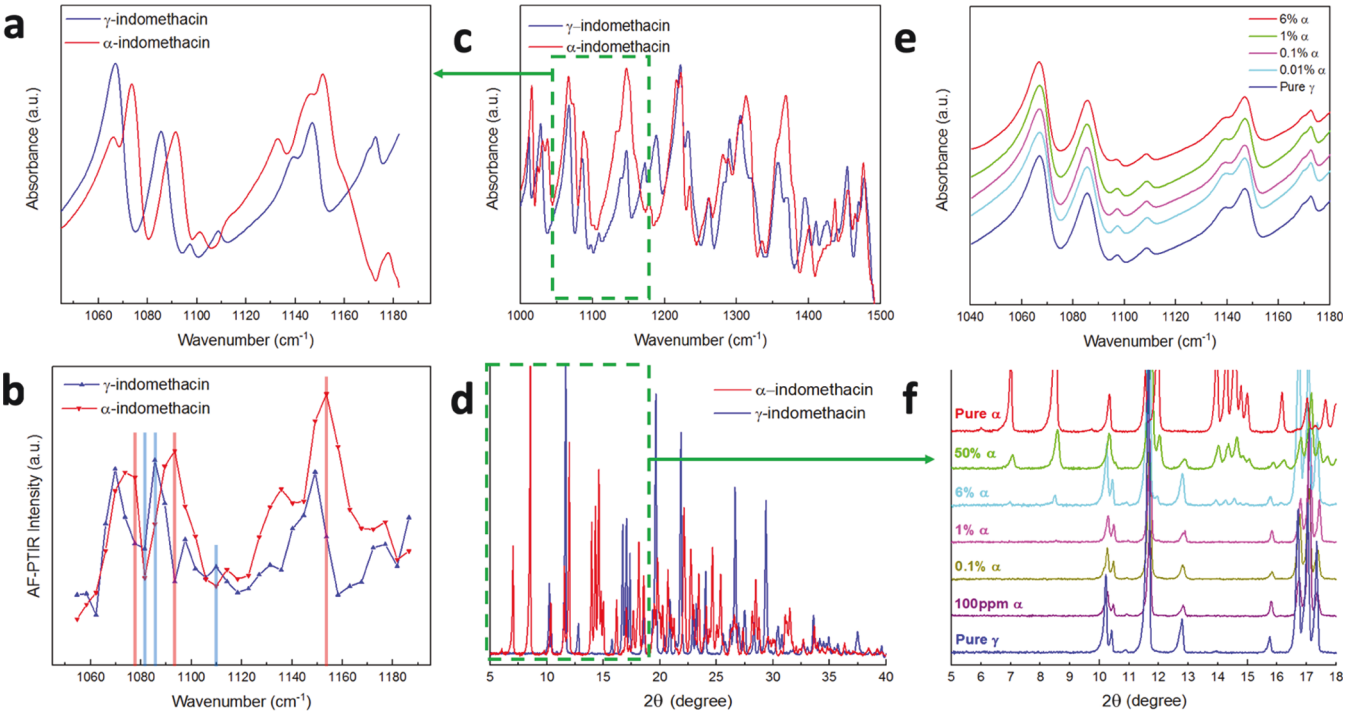

Figure 2. (a, b) FTIR and recovered AF-PTIR spectra of the two indomethacin crystal forms in the region accessible by the QCL array. (c, d) Full fingerprint region FTIR spectra and full PXRD patterns of the two indomethacin crystal polymorphs. (e, f) Dependence of FTIR spectra and PXRD patterns of the mixture of two crystal forms on the α-form concentration.

https://doi.org/10.1021/acs.analchem.2c02358
Anal. Chem. 2022, 94, 13100−13107

AF-PTIR Data Analysis and Crystal Form Assignment. Two spectral sequences were designed to optimally discriminate between the crystal polymorphs of indomethacin based on the differences in their mid-IR absorption spectra (Figure 2a,b). Each of the individual sequences consisted of three QCL spectral channels fired in a rapid burst pattern (30 ns delay between pulses). The channels were initially selected based on a non-negative matrix factorization optimization procedure[30] described in the Supporting Information, followed by manual down-selection to a subset of the three most significant channels to aid in discrimination between crystal polymorphs. QCL channels centered at 1081, 1085, and 1109 cm^{-1} (indicated by vertical blue lines in Figure 2b) were used in the sequence optimized for γ-form mid-IR absorption (γ-sequence), while channels at 1077, 1093, and 1153 cm^{-1} (vertical red lines in Figure 2b) were used in the α-sequence. The NMF algorithm generally selected channels that maximized the ratio of signal intensities for the two polymorphs. When down-sizing the spectral masks, preference was given to the channels that (i) corresponded to the highest ratio in AF-PTIR intensity for each of the polymorphs and (ii) corresponded to QCL channels with higher average power to achieve higher SNR. Using a larger number of individual spectral channels within each sequence resulted in a reduction in the contrast between AF-PTIR images due to the highly overlapping nature of the components' mid-IR spectra.

Each particle within an FoV was classified as either an α- or γ-indomethacin particle. Two AF-PTIR measurements were collected at each FoV using the two QCL sequences described above. The FoV was first segmented into superpixels, with each superpixel corresponding to a single spatially isolated particle. The relative concentration of each crystal phase was calculated for each superpixel using the computational approach described for F-PTIR analysis previously (detailed in the Supporting Information).[27] Each superpixel was assigned to one of the two present crystal forms according to the shortest spectral Euclidean distance to the mean spectrum of a given class. False-colored images were plotted based on this assignment.

Large Field-of-View TPE-UVF and SHG Imaging. Statistical evaluation of the SHG-active domains within an FoV was performed on TPE-UVF and SHG images collected using a commercial beam-scanning nonlinear optical microscope (Formulatrix SONICC). The vendor software (Rock Imager) was used for image collection. TPE-UVF images were collected in epi configuration with 532 nm excitation, with an average incident power of 3.5 mW. SHG images were collected in transmission mode using a 1064 nm incident beam with an average laser power of 100 mW at the sample plane.

Powder X-ray Diffraction Measurements. PXRD measurements were conducted using a Panalytical Empyrean diffractometer at room temperature with Cu Kα radiation. Diffraction patterns for all indomethacin samples were collected in the 2θ angle range of 5−40°. Reference patterns of α- (CCDC 814524) and γ- (CCDC 1180373) crystal forms were used to fit the experimental diffraction pattern by Rietveld analysis.

FTIR Measurements. All FTIR measurements were conducted using a Thermo Nicolet Nexus 470 spectrometer in the reflectance configuration. The spectral resolution for all collected spectra was 1 cm^{-1}.

Materials and Sample Preparation. Commercial indomethacin powder (Letco Medical USP, 685406) contained only γ-indomethacin crystal form, as was confirmed by PXRD. Metastable α-form was prepared by following the procedure suggested by Kaneniwa et al.[31] Specifically, a powder of γ-form crystals was dissolved in hot ethanol to make a saturated solution. Crystals of α-indomethacin were rapidly precipitated by adding room temperature distilled water, followed by filtration. The produced crystals were characterized by PXRD and FTIR (Figure 2).

A powdered sample containing 1% m/m concentration of the α-form crystals in γ-form was prepared by physical mixing using a mortar and pestle. The samples containing 0.1% and 100 ppm by mass of α-indomethacin were prepared by diluting the 1% mixture.

RESULTS AND DISCUSSION

Characterization of the Pure Components. The crystal form composition of the commercial indomethacin powder was characterized by PXRD. Indomethacin is marketed in crystalline solid dosage forms containing only the non-centrosymmetric γ crystal polymorph. Consistent with expectations, the PXRD diffraction of the pure commercially available indomethacin powder showed only peaks characteristic of the γ crystal form (blue curve in Figure 2d). Rietveld analysis further excluded the presence of detectable impurities (e.g., centrosymmetric α-form crystals). The powder diffraction pattern of the prepared α-polymorph crystals is shown in Figure 2d (red curve). More detailed results of the Rietveld analysis are provided in the Supporting Information. PXRD patterns of a series of samples that consisted of predominantly γ-indomethacin crystals with varying concentrations of the α-form crystals are shown in Figure 2f. Most of the α-phase diffraction peaks were still clearly visible at 6% concentration but were nearly undetectable at 1% concentration, which is around the LoD for the method. None of the α-form peaks were visible for mixtures with a mass concentration below 1%.

FTIR spectroscopy of the two studied indomethacin crystal polymorphs revealed noticeable differences in their mid-IR absorption spectra. Fingerprint region spectra of both pure crystal polymorphs are shown in Figure 2c. The green box in Figure 2c highlights the region covered by the QCL array, and the zoom-in spectra in this region are shown in Figure 2a. The presence of α-indomethacin impurity at concentrations up to 6% m/m did not cause any noticeable change to FTIR spectra of the γ crystal form, as demonstrated in Figure 2e. The mid-IR spectra of the γ-form and α-form produced substantial spectral differences within the accessible range of the QCL, suggesting that the two crystal forms potentially could be discriminated by AF-PTIR microscopy. The recovered AF-PTIR spectra of individual crystal forms prepared and analyzed as pure powders are shown in Figure 2b. While generally in good agreement, subtle differences in peak positions and amplitudes arose between the FTIR and AF-PTIR spectra. The apparent variations in intensities of some peaks are tentatively attributed to a combination of two factors: (i) preferred orientation effects from the finite number of crystals accessible within the AF-PTIR FoV, and (ii) the lower signal-to-noise ratio and spectral resolution accessible by the 32-channel QCL array used for the AF-PTIR measurements.

SHG microscopy enabled microscopic discrimination between the studied polymorphs due to their different crystal symmetry. The γ-form commonly used in commercially available final dosage forms is composed of centrosymmetric crystals with the $P_{\bar{1}}$ space group. Coherent second harmonic

https://doi.org/10.1021/acs.analchem.2c02358
Anal. Chem. 2022, 94, 13100−13107

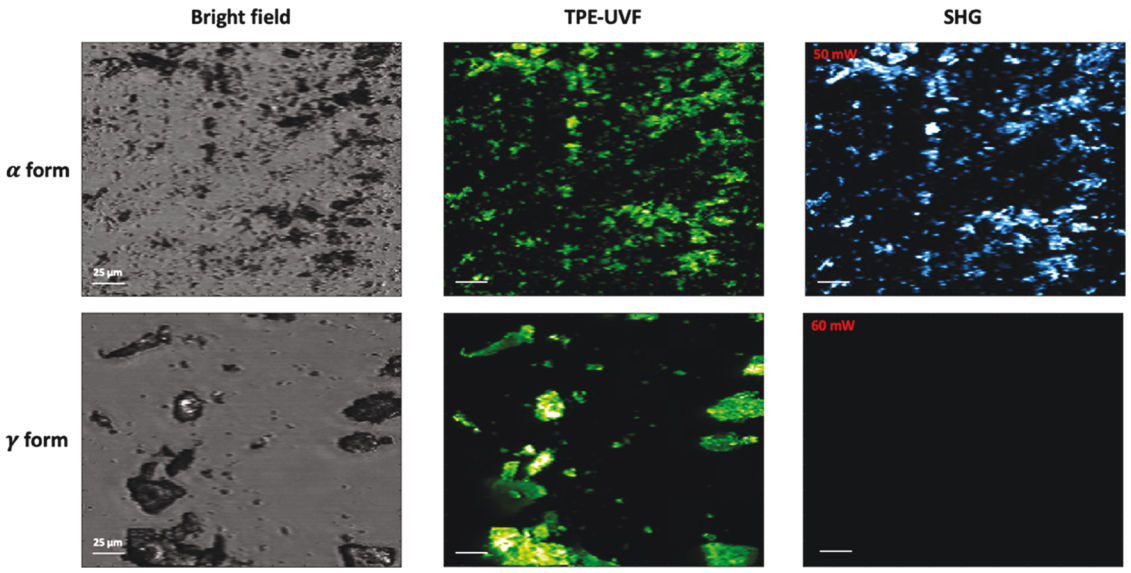

Figure 3. Bright field, TPE-UVF, and SHG images of pure powders of α- and γ-indomethacin crystals.

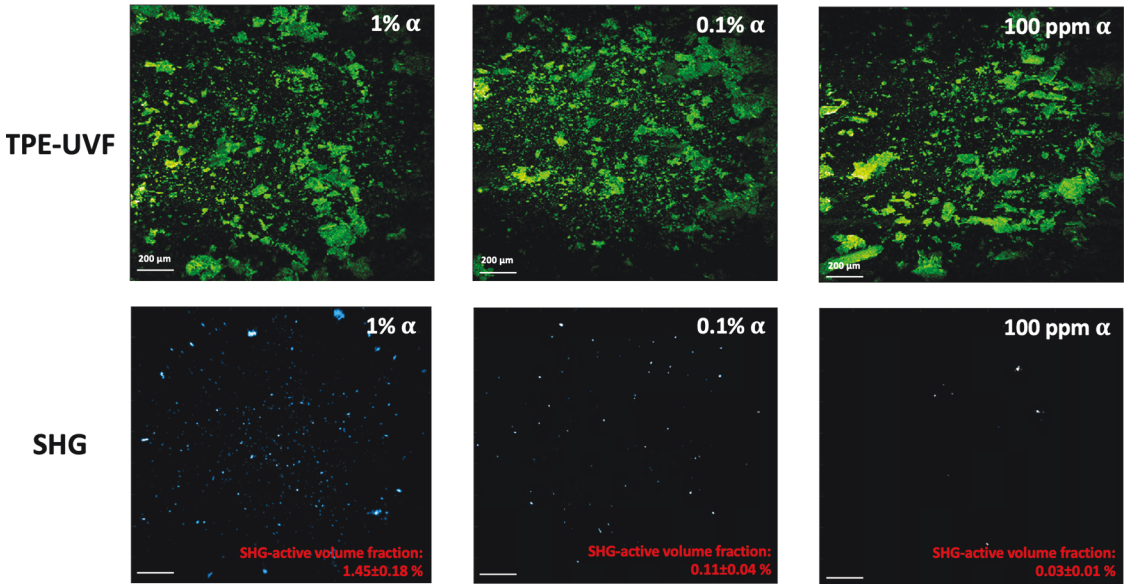

Figure 4. TPE-UVF and SHG images of the representative FoVs for the crystal forms mixture with different concentrations of α-indomethacin.

generation is symmetry-forbidden for centrosymmetric space groups. Consistent with this expectation based on symmetry, no detectable SHG activity was observed for pure γ-indomethacin powder, as demonstrated in Figure 3. In contrast, the metastable α-polymorph adopts a $P2_1$ non-centrosymmetric space group. Strong SHG was observed from all crystals within an FoV for the sample containing only α-indomethacin (Figure 3). Moreover, both crystal forms exhibited strong TPE-UVF, consistent with a previous report indicating bright TPE-UVF activity per unit volume for indomethacin.[29]

Qualitative and Quantitative Characterization of the Mixtures of Two Crystal Forms. A concentration series of solid mixtures of α- and γ- indomethacin was prepared to investigate the LoD of the AF-PTIR microscopy for comparison with routine commercially available methods. The mixtures containing 1, 0.1, and 0.01% (100 ppm) mass fractions of α-indomethacin particles were studied with TPE-UVF and SHG microscopy. Large FoV (2 mm × 2 mm) measurements were conducted to quantitatively assess the volume fraction of SHG-active particles within the prepared mixtures. Representative TPE-UVF and SHG images are shown in Figure 4. The total volume of the SHG-active phase was calculated by treating every segmented particle in the SHG images as spheroidal for volume estimation, consistent with prior work for small particles.[32] Corresponding TPE-UVF images were acquired to calculate the total volume of all indomethacin particles within the same FoV. The total volume of TPE-UVF active particles was given a product of the total particle area by the depth of field (20 μm), as was previously suggested for powders analysis by Chowdhury et al. in the limit of large particles.[33] The relative concentrations of the SHG-active impurity were calculated for each sample after averaging over six different FoVs. To minimize computational bias, data from FoVs containing large (>50 μm) nonspheroidal SHG-bright particles were manually excluded from the analysis.

https://doi.org/10.1021/acs.analchem.2c02358
Anal. Chem. 2022, 94, 13100−13107

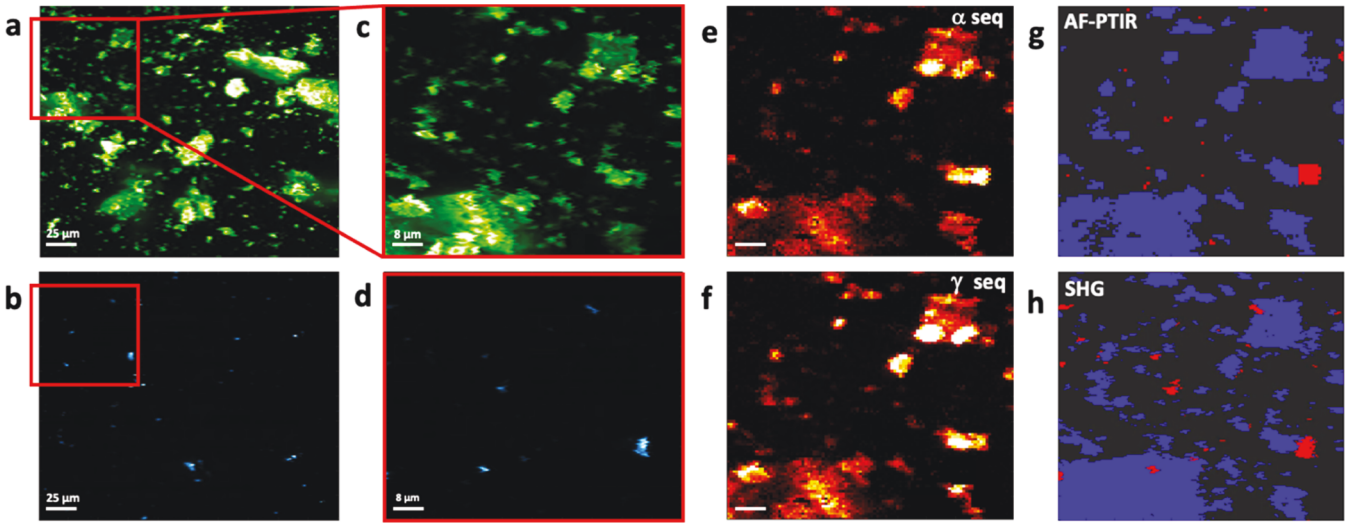

Figure 5. AF-PTIR microscopy of the sample containing 0.1 mass % of α-indomethacin. (a, b) TPE-UVF and SHG images of the large FoV. (c–f) TPE-UVF, SHG, and AF-PTIR images of the selected smaller FoV. (g, h) Independently obtained crystal form assignments of individual crystals with the FoV based on AF-PTIR and SHG microscopy. Pixels assigned to the γ-form are shown in blue, while the pixels assigned to the α-form are shown in red.

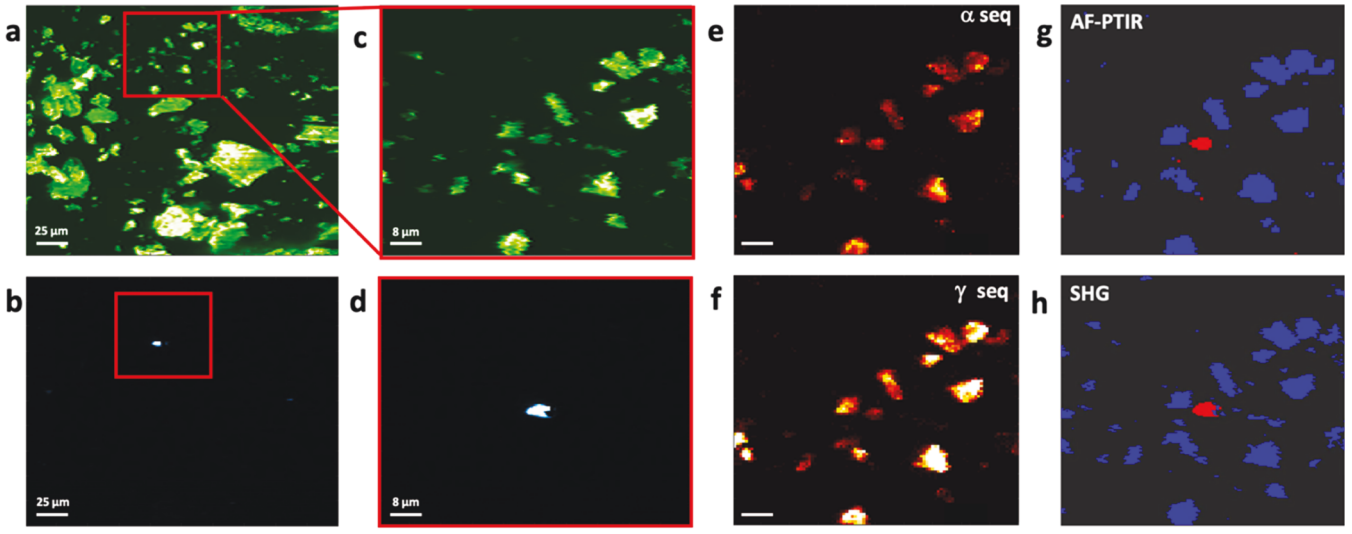

Figure 6. AF-PTIR microscopy of the sample containing 100 ppm by mass of α-indomethacin. (a, b) TPE-UVF and SHG images of the large FoV. (c–f) TPE-UVF, SHG, and AF-PTIR images of the selected smaller FoV. (g, h) Independently obtained crystal form assignments of individual crystals with the FoV based on AF-PTIR and SHG microscopy. Pixels assigned to the γ-form are shown in blue, while the pixels assigned to the α-form are shown in red.

Following the rejection of these outliers, the average SHG intensity per unit volume was used to estimate the SHG-active phase volume for the FoVs containing large nonspherical particles. The volume fractions of SHG-active materials are given in the bottom right corners of SHG images in Figure 4.

AF-PTIR Microscopy of Indomethacin Crystal Forms Mixture Samples. AF-PTIR microscopy, in combination with rapid SHG imaging, was applied to detect individual crystals of the α-form in γ-indomethacin samples. AF-PTIR was performed using 1, 0.1, and 0.01% (100 ppm) mass fractions of α-indomethacin. To reduce the total analysis time, larger FoV (300 μm × 300 μm) SHG images were acquired before AF-PTIR analysis (Figures 5a,b and 6a,b). The comparatively fast acquisition time for SHG images (20 s per image) was used to help guide the selection of smaller FoVs (70 μm × 70 μm) around regions of interest for targeted analysis by AF-PTIR (Figures 5c,d and 6c,d). The resulting AF-PTIR images for two QCL sequences and the false-color crystal form assignment images are shown in Figure 5e–g for the 0.1% sample, and in Figure 6e–g for the 100 ppm sample. Additionally, the AF-PTIR results are provided in the Supporting Information for the 1% sample. In all cases, targeted AF-PTIR measurements were performed on the FoVs that were initially identified by SHG imaging of the larger sample regions, as shown by red boxes in Figures 5 and 6. Furthermore, SHG microscopy results within the smaller FoVs were used to independently evaluate the AF-PTIR assignments of individual crystals to either α or γ crystal form. False-colored composite images of TPE-UVF and SHG activity within each smaller FoV are shown in Figures 5h and 6h.

https://doi.org/10.1021/acs.analchem.2c02358
Anal. Chem. 2022, 94, 13100–13107

DISCUSSION

AF-PTIR microscopy enabled the detection of α-indomethacin with limits of detection significantly lower than analysis of the same material using laboratory-scale PXRD instrumentation. The limits of detection for both methods were estimated based on the collected experimental data. For PXRD, it was calculated that the most prominent diffraction peak of the α-form at 8.3° could be resolved with the SNR ratio of at least 3 at the lowest concentration of 0.99%, which is consistent with the commonly accepted LoD for this method. For AF-PTIR, based on the obtained signal per unit volume and noise standard deviation values for the images collected for the 100 ppm sample, the LoD was calculated to correspond to the detection of a 0.16 μm^3 single particle within an 80 μm × 80 μm FoV. Given the average FoV occupation by particles of 15%, this corresponds to a 5 ppm volume fraction limit of detection.

The accuracy of AF-PTIR spectroscopic per-particle crystal form assignment was independently assessed by SHG microscopy, as shown in Figure 5. In this particular case, the two crystal forms of indomethacin studies fortuitously exhibit substantial differences in SHG activity, providing an independent means for polymorph assignment. As discussed above, only noncentrosymmetric crystals of the α-indomethacin generated detectable SHG signal in the particular case studied herein. The good agreement between the false-colored images obtained independently by AF-PTIR and SHG microscopy supports the accuracy of chemical assignments made by AF-PTIR analysis. SHG-guided measurements were previously shown to lower LoDs for synchrotron X-ray diffraction and Raman spectroscopy.[34] However, synchrotron XRD requires access to specialized facilities. While Raman spectroscopy is highly sensitive to chemical composition and structure, increasing complex samples can benefit from multiple independent analysis methods. AF-PTIR analysis could potentially provide another "arrow in the quiver" as a method capable of ppm level discrimination between APIs crystal forms based on their fingerprint region mid-IR absorption.

AF-PTIR further expands the scope of microspectroscopy tools for chemical classification in multimodal microscopy. In the present study, the compatibility of AF-PTIR with TPE-UVF and SHG microscopy significantly improved the statistical confidence in assignments of crystal form. More generally, the counter-propagating configuration implemented for AF-PTIR supports straightforward multimodal integration with broad classes of complementary methods compatible with epi-detection for crystal form analysis, including spontaneous and coherent Raman spectroscopy (including THz Raman), optically detected PTIR based on detection of thermal modulation of back-scattering, dark-field imaging, and polarization-dependent imaging, including nonlinear optical Stokes ellipsometry enabled by rapid incident polarization modulation.[35−38] Each method has potential advantages and limitations, with overall substantial improvements in classification accuracy arising through the integration of multiple complementary analysis approaches within a single microscopic analysis platform.

CONCLUSIONS

SHG-guided AF-PTIR microscopy was shown to discriminate between different polymorphs of indomethacin based on differences in mid-infrared absorbance, with limits of detection for the metastable α-form of 5 ppm. Multimodal imaging pairing SHG and photothermal microscopy enabled independent confirmation of AF-PTIR for polymorph classification. Early identification of trace crystal form impurities has the potential to inform the design of stable and efficacious final dosage forms of active pharmaceutical ingredients.

ASSOCIATED CONTENT

Supporting Information

The Supporting Information is available free of charge at https://pubs.acs.org/doi/10.1021/acs.analchem.2c02358.

Additional information is provided describing: (i) QCL array parameters, (ii) AF-PTIR data analysis and image generation algorithm, (iii) PXRD refinement data, and (iv) AF-PTIR results for the sample containing 1% impurity of α-indomethacin (PDF)

AUTHOR INFORMATION

Corresponding Author

Garth J. Simpson − *Department of Chemistry, Purdue University, West Lafayette, Indiana 47907, United States;* orcid.org/0000-0002-3932-848X; Email: gsimpson@purdue.edu

Authors

Aleksandr Razumtcev − *Department of Chemistry, Purdue University, West Lafayette, Indiana 47907, United States;* orcid.org/0000-0001-9591-8612

Minghe Li − *Department of Chemistry, Purdue University, West Lafayette, Indiana 47907, United States*

Complete contact information is available at: https://pubs.acs.org/10.1021/acs.analchem.2c02358

Author Contributions

†A.R. and M.L. contributed equally to this work. A.R. and M.L performed experiments and data analysis. G.J.S. managed and supervised the project.

Notes

The authors declare no competing financial interest.

ACKNOWLEDGMENTS

M.L., A.R., and G.J.S. gratefully acknowledge funding from the National Science Foundation (NSF-D3SC-2004046, and CIF-1763896). M.L. and A.R. also acknowledge support from the NSF Center for Bioanalytic Metrology (IIP-1916691). A.R. also acknowledges the Purdue Research Foundation for a Graduate Scholarship.

REFERENCES

(1) Cruz-Cabeza, A. J.; Reutzel-Edens, S. M.; Bernstein, J. *Chem. Soc. Rev.* **2015**, *44*, 8619−8635.

(2) Guo, Z.; Ma, M.; Wang, T.; Chang, D.; Jiang, T.; Wang, S. *AAPS PharmSciTech* **2011**, *12*, 610−619.

(3) Savjani, K. T.; Gajjar, A. K.; Savjani, J. K. *ISRN Pharm.* **2012**, *2012*, No. 195727.

(4) Chemburkar, S. R.; Bauer, J.; Deming, K.; Spiwek, H.; Patel, K.; Morris, J.; Henry, R.; Spanton, S.; Dziki, W.; Porter, W.; Quick, J.; Bauer, P.; Donaubauer, J.; Narayanan, B. A.; Soldani, M.; Riley, D.; McFarland, K. *Org. Process Res. Dev.* **2000**, *4*, 413−417.

(5) Bauer, J.; Spanton, S.; Henry, R.; Quick, J.; Dziki, W.; Porter, W.; Morris, J. *Pharm. Res.* **2001**, *18*, 859−866.

(6) Morissette, S. L.; Stephen, S.; Douglas, L.; J, C. M.; Örn, A. *Proc. Natl. Acad. Sci.* **2003**, *100*, 2180−2184.
(7) Varasteh, M.; Deng, Z.; Hwang, H.; Kim, Y. J.; Wong, G. B. *Int. J. Pharm.* **2009**, *366*, 74−81.
(8) Egusa, K.; Okazaki, F.; Schiewe, J.; Werthmann, U.; Wolkenhauer, M. *Drugs R&D* **2017**, *17*, 413−418.
(9) Lin, W.-Q.; Jiang, J.-H.; Yang, H.-F.; Ozaki, Y.; Shen, G.-L.; Yu, R.-Q. *Anal. Chem.* **2006**, *78*, 6003−6011.
(10) Auer, M. E.; Griesser, U. J.; Sawatzki, J. *J. Mol. Struct.* **2003**, *661−662*, 307−317.
(11) Ford, J. L.; Mann, T. E. *Adv. Drug Delivery Rev.* **2012**, *64*, 422−430.
(12) Bruni, G.; Berbenni, V.; Milanese, C.; Girella, A.; Cardini, A.; Lanfranconi, S.; Marini, A. *J. Pharm. Biomed. Anal.* **2011**, *54*, 1196−1199.
(13) Wanapun, D.; Kestur, U. S.; Kissick, D. J.; Simpson, G. J.; Taylor, L. S. *Anal. Chem.* **2010**, *82*, 5425−5432.
(14) Wampler, R. D.; Kissick, D. J.; Dehen, C. J.; Gualtieri, E. J.; Grey, J. L.; Wang, H.-F.; Thompson, D. H.; Cheng, J.-X.; Simpson, G. J. *J. Am. Chem. Soc.* **2008**, *130*, 14076−14077.
(15) Toth, S. J.; Madden, J. T.; Taylor, L. S.; Marsac, P.; Simpson, G. J. *Anal. Chem.* **2012**, *84*, 5869−5875.
(16) Newman, J. A.; Schmitt, P. D.; Toth, S. J.; Deng, F.; Zhang, S.; Simpson, G. J. *Anal. Chem.* **2015**, *87*, 10950−10955.
(17) Vankeirsbilck, T.; Vercauteren, A.; Baeyens, W.; van der Weken, G.; Verpoort, F.; Vergote, G.; Remon, J. P. *TrAC, Trends Anal. Chem.* **2002**, *21*, 869−877.
(18) Strachan, C. J.; Taday, P. F.; Newnham, D. A.; Gordon, K. C.; Zeitler, J. A.; Pepper, M.; Rades, T. *J. Pharm. Sci.* **2005**, *94*, 837−846.
(19) Schmitt, P. D.; Trasi, N. S.; Taylor, L. S.; Simpson, G. J. *Mol. Pharmaceutics* **2015**, *12*, 2378−2383.
(20) Novakovic, D.; Saarinen, J.; Rojalin, T.; Antikainen, O.; Fraser-Miller, S. J.; Laaksonen, T.; Peltonen, L.; Isomäki, A.; Strachan, C. J. *Anal. Chem.* **2017**, *89*, 11460−11467.
(21) Porquez, J. G.; Slepkov, A. D. *AIP Adv.* **2018**, *8*, No. 095213.
(22) Hartshorn, C. M.; Lee, Y. J.; Camp, C. H.; Liu, Z.; Heddleston, J.; Canfield, N.; Rhodes, T. A.; Hight Walker, A. R.; Marsac, P. J.; Cicerone, M. T. *Anal. Chem.* **2013**, *85*, 8102−8111.
(23) Kazarian, S. G.; Chan, K. L. A. *Analyst* **2013**, *138*, 1940−1951.
(24) Zhang, D.; Li, C.; Zhang, C.; Slipchenko, M. N.; Eakins, G.; Cheng, J.-X. *Sci. Adv.* **2016**, *2*, No. e1600521.
(25) Li, C.; Zhang, D.; Slipchenko, M. N.; Cheng, J. X. *Anal. Chem.* **2017**, *89*, 4863−4867.
(26) Yeran, B.; Jiaze, Y.; Ji-Xin, C. *Sci. Adv.* **2022**, *7*, No. eabg1559.
(27) Li, M.; Razumtcev, A.; Yang, R.; Liu, Y.; Rong, J.; Geiger, A. C.; Blanchard, R.; Pfluegl, C.; Taylor, L. S.; Simpson, G. J. *J. Am. Chem. Soc.* **2021**, *143*, 10809−10815.
(28) Zhang, Y.; Zong, H.; Zong, C.; Tan, Y.; Zhang, M.; Zhan, Y.; Cheng, J. X. *J. Am. Chem. Soc.* **2021**, *143*, 11490−11499.
(29) Razumtcev, A.; Li, M.; Rong, J.; Teng, C. C.; Pfluegl, C.; Taylor, L. S.; Simpson, G. J. *Anal. Chem.* **2022**, *94*, 6512−6520.
(30) Griffin, S. R.; Biechele-Speziale, J. A.; Smith, C. J.; You-Dow, X.; White, J. K.; Zhang, S.-W.; Novak, J.; Liu, Z.; Simpson, G. J. *Anal. Chem.* **2019**, *91*, 5286−5294.
(31) Kaneniwa, N.; Otsuka, M.; Hayashi, T. *Chem. Pharm. Bull.* **1985**, *33*, 3447−3455.
(32) Smith, C. J.; Dinh, J.; Schmitt, P. D.; Stroud, P. A.; Hinds, J.; Johnson, M. J.; Simpson, G. J. *Appl. Spectrosc.* **2018**, *72*, 1594−1605.
(33) Chowdhury, A. U.; Zhang, S.; Simpson, G. J. *Anal. Chem.* **2016**, *88*, 3853−3863.
(34) Newman, J. A.; Zhang, S.; Sullivan, S. Z.; Dow, X. Y.; Becker, M.; Sheedlo, M. J.; Stepanov, S.; Carlsen, M. S.; Everly, R. M.; Das, C.; Fischetti, R. F.; Simpson, G. J. *J. Synchrotron Radiat.* **2016**, *23*, 959−965.
(35) Schmitt, P. D.; DeWalt, E. L.; Dow, X. Y.; Simpson, G. J. *Anal. Chem.* **2016**, *88*, 5760−5768.
(36) Strachan, C. J.; Rades, T.; Lee, C. J. *Opt Lasers Eng.* **2005**, *43*, 209−220.
(37) Muthudoss, P.; Kumar, S.; Ann, E. Y. C.; Young, K. J.; Chi, R. L. R.; Allada, R.; Jayagopal, B.; Dubala, A.; Babla, I. B.; Das, S.; Mhetre, S.; Saraf, I.; Paudel, A. *J. Pharm. Biomed. Anal.* **2022**, *210*, No. 114581.
(38) Li, C.; Zhang, D.; Slipchenko, M. N.; Cheng, J.-X. *Anal. Chem.* **2017**, *89*, 4863−4867.

https://doi.org/10.1021/acs.analchem.2c02358
Anal. Chem. 2022, 94, 13100−13107